ADVANCED FUNCTIONAL MATERIALS
www.afm-journal.de

Engineering Vascular Self-Assembly by Controlled 3D-Printed Cell Placement

*Isabel Orellano, Alexander Thomas, Aaron Herrera, Erik Brauer, Dag Wulsten, Ansgar Petersen, Lutz Kloke, and Georg N. Duda**

Nutrient supply via a functional vasculature is essential during regenerative processes, tissue growth, and homeostasis. 3D bioprinting offers the opportunity to engineer vascularized constructs by combining cells and biocompatible materials in specifically designed fashions. However, the complexity of microvascular dynamic networks can hardly be recapitulated yet, even by sophisticated 3D manufacturing. Ideally, the natural organizational competences of endothelial cells will be harnessed such that engineered vascular networks self-assemble to form complex, controllable microvascular patterns. Here, a bioengineering approach is presented to control microvascular structure formation and to steer cellular self-assembly of endothelial and supporting cells within a multi-material stereolithographic 3D bioprinting concept. Bioengineered vascularized constructs are generated by controlled cell deposition in an enzymatically degradable or a non-degradable material. In vitro, the microvascular structures are regulated in distribution, network orientation, vessel length and branching behavior and developed lumen, signs of vascular stabilization and an interconnected vascular network including anastomosis. This novel biofabrication approach demonstrates the capability to control microvascular network formation by using cellular and spatial cues allowing the generation of distinctly yet precisely vascularized constructs. Such novel approach of controlled microvascular formation may play a fundamental role in the development of vascularized implants or in vitro screening models.

1. Introduction

Vascularization is not only essential for organogenesis, tissue formation, and maintenance, but also key in healing and regeneration as endothelial cells play a central role upon disease, injury, and infection.[1] Physiological vascularization is characterized by a highly organized, tissue-specific, and hierarchically structured network.[2] In situations in which insufficient vascularization impedes healing, bioengineering technologies can help to induce regeneration by enhancing basic cellular mechanisms relevant for vascular formation. Rapid vascularization is key to sufficiently provide nutrients, oxygen, and signaling factors, and to transport metabolites. All these necessary processes ensure cell survival and prevent the development of a necrotic core in larger tissue or organ settings.[3–5] Unfortunately, mimicking the physiological complexity of tissues and microvasculature, including cell arrangement and extra-cellular matrix (ECM) interactions, remains a challenge for in vitro approaches.[3–6] Vasculature of distinct tissues is characterized by specific vascular patterns, which differ greatly across tissues.[7–11] Thus, controlling a distinct patterning process of vascularization appears essential to bioengineer physiological supply and ensure gross functionality of tissues.

A variety of approaches has been developed aiming to fabricate functional 3D-vascularized constructs: One strategy is to generate endothelial surfaces or preformed primitive vessels,[5,12] and to initiate angiogenic sprouting from these defined structures.[3,13,14] A different strategy is to rely on the intrinsic self-assembly potential of cells to form microvascular structures, frequently by co-cultivating endothelial cells (ECs) with a supporting mural

I. Orellano, A. Herrera, E. Brauer, D. Wulsten, A. Petersen, G. N. Duda
Julius Wolff Institute
Berlin Institute of Health at Charité – Universitätsmedizin Berlin
Augustenburger Platz 1, 13353 Berlin, Germany
E-mail: georg.duda@charite.de

The ORCID identification number(s) for the author(s) of this article can be found under https://doi.org/10.1002/adfm.202208325.

DOI: 10.1002/adfm.202208325

I. Orellano, A. Herrera, E. Brauer, D. Wulsten, A. Petersen, G. N. Duda
Berlin Institute of Health Center for Regenerative Therapies
Berlin Institute of Health at Charité – Universitätsmedizin Berlin
Augustenburger Platz 1, 13353 Berlin, Germany

I. Orellano, A. Petersen, G. N. Duda
Berlin-Brandenburg School for Regenerative Therapies
Charité – Universitätsmedizin Berlin
Augustenburger Platz 1, 13353 Berlin, Germany

I. Orellano, A. Thomas
Technische Universität Berlin
Department of Medical Biotechnology
Gustav-Meyer-Allee 25, 13355 Berlin, Germany

A. Thomas, L. Kloke
Cellbricks GmbH
Müllerstraße 178, 13353 Berlin, Germany

cell type.[7,15,16] While human umbilical vein ECs (HUVECs) are widely used for such approaches due to their good availability and high degree of characterization,[17] human mesenchymal stromal cells (hMSCs) represent the most common supportive cell type because of their differentiation and pro-angiogenic potential, as well as their well-studied capacity of inducing the formation of vascular structures.[4,15,18,19] Although the strategy of generating preformed vessels with endothelial lining allows control over vessel geometry, reproducing the complexity of naturally occurring microvascular networks remains challenging.[3,10,20] Moreover, producing vessel analogs by endothelial lining fail to reconstitute the physiological endothelial morphogenesis process of forming lumenized structures. On the other hand, current 3D bioprinting strategies that aim to induce endogenous microvascular self-assembly, result in microvascular network formation with limited control over its exact patterning.

Here, we introduce a bioengineering approach that combines the above-mentioned strategies in a novel way such that geometry of microvascular structures could be controlled by using a multi-material projection-based stereolithography 3D bioprinter and an innovative biomaterial system.[21] Within its frame, the angiogenic and vasculogenic behavior of HUVECs was studied in interplay with hMSCs and human dermal fibroblasts (hdFs) as supporting cell types. Therefore, this work represents a systematic investigation of the formation and modulation of microvascular structures via cellular self-assembly by altering cell type and placement. Our findings reveal not only that the direct printing and posterior self-assembly of an endothelial lining is possible, but also how cell type and position can direct the formation of self-assembled microvascular structures within the construct. In addition, we were able to engineer defined compartments for the formation of microvascular structures. The application of these findings could facilitate the development of new tissue engineering strategies with optimized vascular structures specifically targeted to tissue demands.

2. Results

2.1. Endothelial Cells Alone Form an Endothelial Lining in the Channel and Migrate into a Distinct Invasion Region

We first aimed at investigating the feasibility of 3D bioprinting to generate vascularized sheets with distinct compartments with and without vascular structures (**Figure 1**a–d). The printing fidelity was high in the *xy*- direction with a relative error of maximum 3%. The lower values in the dimensions of the construct can be a consequence of cellular traction forces as early as 2 days after printing (Figure 1e,f and **Table 1**).[22] The greater relative error in *z*-direction (height) was a result of the lower resolution of the 3D bioprinter (100 µm) that defines the thickness of each layer.

The properties of the bulk biomaterial methacrylated gelatin (GelMA) were chosen to ensure cell-cell communication and the ability for supporting cell migration out of the bulk while at the same time impeding the invasion of microvascular structures, thereby guiding them toward specifically designed geometrical compartments. To facilitate this, a soft material was selected. Material testing revealed a mean E-modulus of 7% w/v GelMA of 1.75 ± 0.07 kPa (mean ± SD) and of 1.5% w/v) methacrylated hyaluranic acid (HAMA) of 3.15 ± 0.16 kPa[21] (Figure 1g). In addition, the effective E-modulus (E_{eff}) of printed constructs with 7% (w/v) GelMA was measured using a nanoindentation device (Piuma Inc., Optics11). We observed the local stiffness of 2.9 ± 1.7 kPa, which is in the range of the bulk properties. Stress relaxation, indicated by the half-time of relaxation ($\tau_{1/2}$), revealed values of 1.7 ± 0.4 s, what is in the range of coagulated bone marrow and fracture hematoma, and has been shown to facilitate cell spreading (exemplary relaxation plot Figure S1, Supporting Information).[23]

Within the constructs, designated vascular compartments consisted of the printed channels and an invasion region between channels that allowed eased cell migration. The 3D layer-by-layer printing technique (Figure 1a,b) enabled the realization of different cellular arrangements (Figure 1c,d) of the invasion region at the resulting interface of the base and top layer of GelMA and in between printed channels (**Figure 2**a). Cells and newly forming microvascular structures were restricted by biological and geometrical cues to the bioprinted channels, the invasion regions, and material properties. These compartments are exemplarily illustrated for the HU-mono group (Figure 2b).

During the bioprinting process, HUVECs were embedded in the channel with the sacrificial ink HAMA, which was then enzymatically degraded within a few hours (Figure 2a, top).[21] After degradation, cells first attached to the channel surfaces and then migrated and populated the invasion region connecting neighboring channels, but without penetrating the GelMA bulk (Figure 2a bottom). This process was confirmed by confocal images of the group HU-mono where HUVECs attached to the inner surface of the printed channels after 2 days of cultivation (Figure 2c). After 10 days of printing, the inner surfaces of the channels were fully covered with an endothelial lining, representing a preformed endothelialized channel with a size of ≈200 µm (Figure 2d). Front view images confirmed the coverage of cells on the available inner surface areas and their attachment to the inner wall of the printed channel, while keeping an open lumen (Figure 2e,f). In the invasion region, however, the presence of cells was very limited after 2 days, highlighting on one hand the precision of the printing method and on the other hand the migration capability of the HUVECs from the channel toward the invasion region. 10 days after printing, HUVECs completely covered the invasion region, connecting the neighboring channels across the invasion region. These first findings validated the printing method and the selection of biomaterials, facilitating the creation of channels by mean of sacrificial ink and the subsequent lining of the surfaces by the cells initially embedded within.

2.2. Co-Culture of HUVECs with hMSCs Facilitates the Formation of a Microvascular Network

Utilizing the advantage of bioprinting to control cell placement in a precise manner, a supporting cell type, here hMSCs, was printed together with the HUVECs in the channel region.

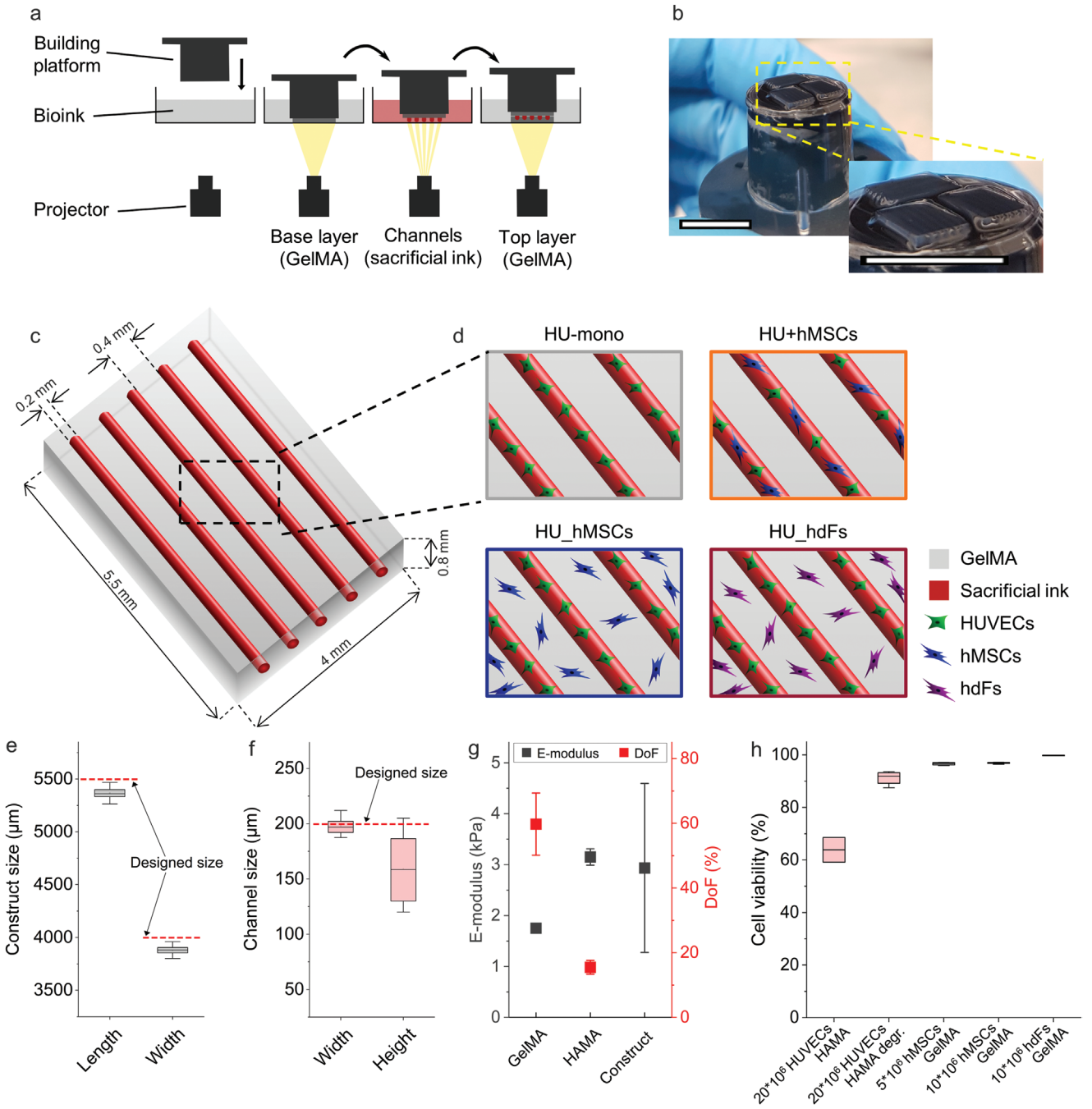

Figure 1. Experimental setup of the 3D-bioprinted vascularized constructs. a) Schematic representation of the printing process with the projection-based stereolithography 3D bioprinting using a multi-material, layer-by-layer printing approach. Hollow channels were generated by enzymatically degrading the sacrificial ink methacrylated hyaluronic acid (HAMA, red) in combination with methacrylated gelatin (GelMA, bulk material, grey). b) Image of constructs after printing on top of the building platform. Scale bars: 10 mm. c) Model of the designed construct with five parallel channels (realized by the printing of sacrificial ink, red) surrounded by a hydrogel (GelMA, grey). d) Illustration of the different investigated cellular arrangements. Printing fidelity of the stereolithographic 3D bioprinter was determined by comparing e) the measured printed hydrogel construct size in length and width and f) the measured channel size in width and height to the designed size in the CAD model (dashed red line, $n = 11$). g) Both bioink materials and the printed construct properties were characterized by their Young's modulus of photopolymerized GelMA ($n = 9$) and HAMA ($n = 3$) and their degree of functionalization (DoF) (HAMA $n = 2$, GelMA $n = 4$). The effective E-modulus of printed constructs was also measured using a nanoindentation method (Piuma Optics11, $n = 4$). h) Cell viability was determined for each cell type at respective cell concentration and in the respective bioink. HUVECs were printed with 20×10^6 cells mL^{-1} in HAMA and measured encapsulated in the photopolymerized ink as well as after degradation of the HAMA with the enzyme hyaluronidase (Hase, HAMA degr.). hMSCs and hdFs were printed in 7% (w/v) GelMA at different cell concentrations ($n = 4$).

By bioprinting hMSCs jointly with HUVECs in the sacrificial channel ink in a cell ration of 1:1 (group HU+hMSCs), direct cell-cell contacts were permitted after enzymatic degradation. Within the initial 2 days, HUVECs and hMSCs formed

Table 1. Dimensions of 3D bioprinting constructs defining printing fidelity.

	Construct length	Construct width	Channel width	Channel height
Designed dim. in µm	5500	4000	200	200
Measured dim. in µm	5368 ± 59	3879 ± 45	198 ± 7	159 ± 30
Absolute error in µm	132 ± 59	121 ± 45	1.9 ± 7.2	41 ± 30
Relative error in %	2.40	3.02	0.95	20.55

multicellular clusters, elongated and formed network junctions within the channels, which are characteristics of vasculogenesis (**Figure 3**a).[6] Over time, microvascular structures developed, forming more mature, strongly aligned and longer microvascular structures in the channels (Figure 3b). The front view representation illustrated that HUVECs and hMSCs

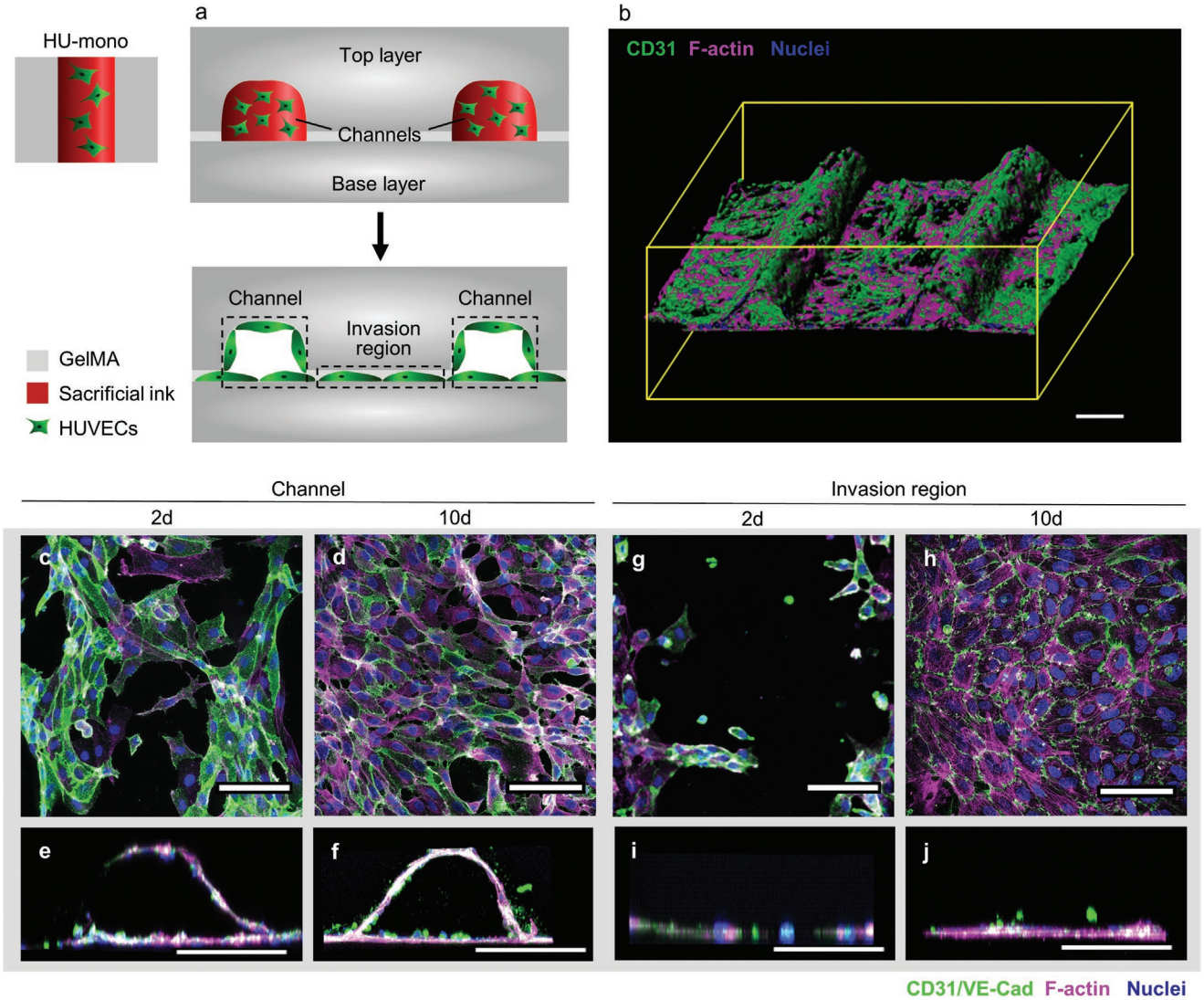

Figure 2. Cellular behavior in case of monoculture of HUVECs (HU-mono) forming a macrovascular channel by endothelial lining. a) Schematic illustration of cells directly after printing encapsulated in the sacrificial ink (red, HAMA, top image) and after enzymatic degradation of the sacrificial ink: cells cover the surface of the channel and migrate into the invasion region between two printing layers, without bulk (grey, GelMA) penetration (lower image). b) Reconstructed confocal image and surface rendering using Imaris (Bitplane) depicting location of channels with endothelial lining and the invasion region covered with endothelial cells in the printed construct 10 days after printing. c,d) Representative confocal images of HUVECs in the channel region 2 and 10 days post printing and e,f) front view images reconstructed with Imaris (Bitplane) showing the complete coverage and endothelial lining of the printed channel. g,h) Representative confocal images of the invasion region 2 and 10 days after printing illustrating the migration of HUVECs. i,j) Front view reconstruction depicting absence of cells in the bulk material. b,j) Samples were stained for F-actin (magenta), and nucleus (blue) and (c–g,i) CD31 to identify endothelial cells (green) or (h,j) VE-Cadherin (green) depicting adherence junctions. Scale bars: b,e,f,i,j) 200 µm, c,d,g,h) 50 µm.

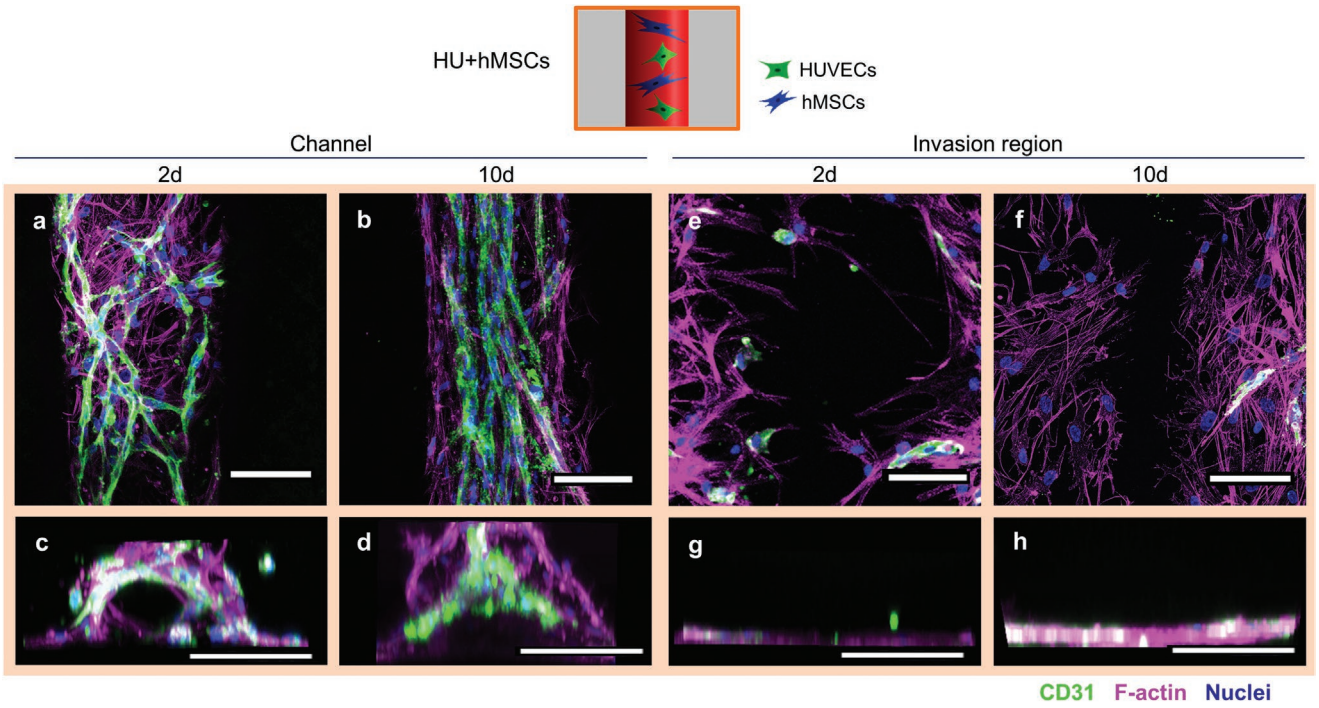

Figure 3. Cellular arrangement of HUVECs and hMSCs printed in proximity in the channel (Group HU+hMSCs). a) Representative confocal images of the channel with HUVECs (green) forming vascular structures as early as 2 days post printing. hMSCs (magenta) in proximity spanning in between newly forming vascular structures. b) Representative confocal image after 10 days showing more mature microvascular structures, with a constant diameter and hMSCs aligning with the strongly oriented vascular structures along the channel direction. c) Representative front view image of the channel 2 days after printing with cells initially attach to channel surface. d) Representative front view image of the channel 10 days after printing completely filled by cells. e,f) Representative images of the invasion region 2 and 10 days after printing with little immigration of HUVECs, but strong immigration of hMSCs from the channel. g,h) Front view reconstructions of the invasion region 2 and 10 days after printing with no cells penetrating the bulk material. Samples were stained for CD31 (HUVECs, green), nuclei (blue) and F-actin (hMSCs and HUVECs, magenta). Scale bars: a,b,e,f) 50 µm, c,d,g,h) 200 µm.

progressively filled most of the channel volume (Figure 3c,d). Only few HUVECs migrated into the invasion regions, but many hMSCs were observed migrating into the region after 2 days already, almost populating the complete region after 10 days (Figure 3e,f). Remarkably, the presence of cells and microvascular structures were mostly restricted to the channel (Figure 3c,d) and invasion region (Figure 3g,h), and were not able to penetrate the GelMA bulk material in a significant manner, creating restricted, distinctly designed regions for invasion.

The striking differences between the groups HU-mono and HU+hMSCs were revealed by the distinct HUVECs morphology and microvascular arrangement (**Figure 4**a,b). While HU-mono tended to initially line the channel and progressively the invasion region, HU+hMSCs lead to a rapid microvascular self-assembly and their location was mostly restricted to the channels. Quantitative analysis of the orientation distribution of the CD31 signal (HUVECs) was conducted to investigate whether the geometrical cue, presented by the printed channel, is able to direct the formation of microvascular structures. The addition of hMSCs not only led to the formation of a microvascular structure but also resulted in a progressive and significantly stronger alignment in direction of the channel (0°) compared to the HUVECs printed alone (Figure 4c). This pointed out that the addition of a supporting cell type facilitates microvasculature self-assembly, while the orientation of the vascular network can be controlled by the geometry of the channel.

Cellular and microvascular migration and proliferation in the two compartments were quantified by the cell coverage, i.e., by measuring the area cells occupied over time. The mean HUVEC coverage (HUVEC area/total area) for the HU-mono group progressively increased from day 2 up to day 10, where they almost covered the complete available surface in the channel (Figure 4d, grey bars). In the HU+hMSCs group, HUVEC coverage within the channel did not significantly increase from day 2 to 10, as the self-assembled microvasculature rapidly organized and populated the available space forming aligned structures (Figure 4d, full orange bars). Additionally, a mild increase of hMSCs was observed over time in the channel (Figure 4d, orange patterned bars). Important parameters to characterize and compare vascular structures are the vessel length and the amount of branching points, which also indicate the process of angiogenesis (sprouting). Considering the vessel length density (VLD = vessel length/volume) in the group HU+hMSCs, premature vascular structures were forming as early as 2 days in the channel (Figure 4b,f) and almost doubled after 10 days. The branch point density (BPD = number of branching points/volume) remained rather constant in the channels (Figure 4h). No microvascular structures were formed in the group HU-mono in the channels (Figure 4f,h),

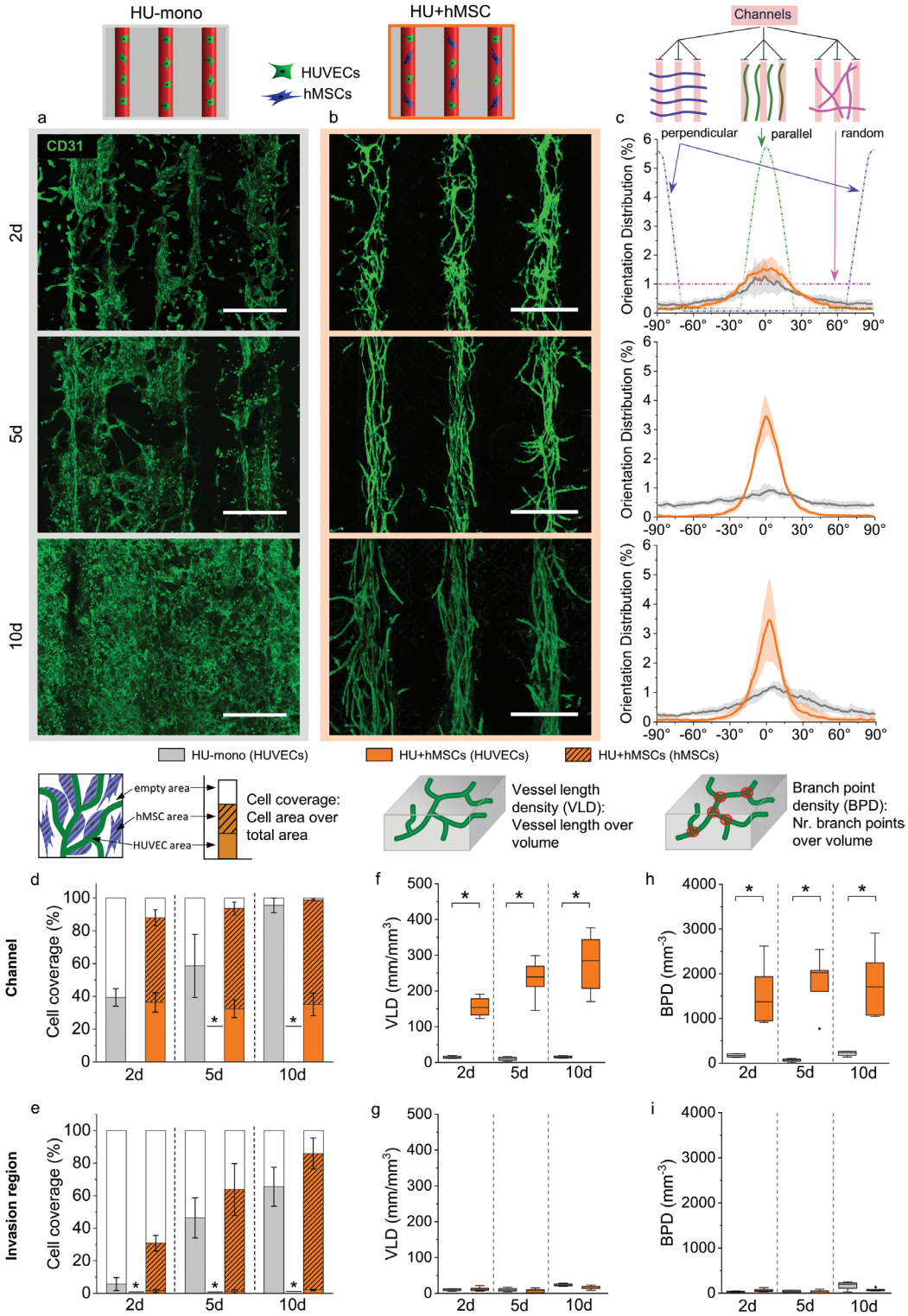

Figure 4. The formation of structured microvascular networks with the addition of a second cell type. Comparison between the group a) HU-mono (grey) and b) HU+hMSCs (orange) visualized by maximum projection of representative confocal images stained for CD31 (green) for 2, 5, and 10 days post printing. Scale bars: 500 µm. c) Cell/Vascular orientation within the channel. c, top) A predominant –90/90° angle represents an orientation of vasculature perpendicular to the axis of the channel (blue curve), a predominant 0° angle the orientation parallel to printed channels (green curve), a random orientation is depicted as horizontal line (pink line). d,e) HUVEC coverage (portion of area covered by HUVECs compared to total available area, full grey/orange bar) compared to calculated hMSC coverage (portion of area covered by hMSCs, patterned orange bar), 100% constitutes the total available area (white bar represents empty area, not covered by cells). f,h) Vessel length density (VLD) and h,i) branch point density (BPD) in the channels and invasion regions for 2, 5, and 10 days post printing. Statistical significance via Mann–Whitney test (two sided), $*p < 0.05$, $n = 4$ (HU-mono), $n = 5$ (HU+hMSCs).

highlighting the need of a supporting cell type for the proper development of vascular structures.[4,19]

In the invasion regions, where no cells were originally printed, HUVECs progressively invaded the region in the group HU-mono, reaching a mean coverage of ≈2/3 at 10th day. In the group HU+hMSCs, the forming microvascular structures locally remained within the channel (<3% HUVEC coverage in invasion region). In contrast, a strong migration of hMSCs out of the channel into the invasion region was visible at 10th day (Figure 4e, orange patterned bars). VLD and BPD in the invasion regions were negligible for both groups: in the group HU-mono, no microvascular structures formed, and in the group HU+hMSCs, microvascular structures were almost exclusively formed in the channels (Figure 4g,i). These results indicate that the inclusion of HUVECs and hMSCs in proximity, besides facilitating the formation and alignment of microvascular structures, induced the reclusion of the HUVECs within the channel region. This is assumed to be consequence of the close interaction between ECs and hMSCs that potentially enhances mechanical and biochemical interaction, directing endothelial cells toward the formation of vascular structures instead of migrating and populating the available space.[4,15,19]

2.3. Spatial Separation of HUVECs from hMSCs Leads to Increased Microvascular Network Complexity in an hMSC Dose-Dependent Manner

It has been shown that the distance between HUVECs and hMSCs influences the process of angiogenesis by modulating the cell-cell communication, including paracrine signaling and cell-cell contacts.[24] To investigate the relevance of hMSC placement on HUVECs' self-assembly to microvascular networks, the influence of local separation of the cell types and hMSC concentration was analyzed. For this, hMSCs were printed into the GelMA bulk material, spatially separated from HUVECs in the channel (group HU_hMSCs). The distinct positioning of the two cell types in bulk and channels was validated 18 h after printing (Figure S2, Supporting Information).

Two different hMSC concentrations (5×10^6 and 10×10^6 hMSCs mL^{-1}, respectively, HU_hMSCs^{low} and HU_hMSCs^{high}) in the surrounding bulk were investigated, which showed a strong impact on microvascular network formation and patterning. Confocal images of group HU_hMSCs^{low} of the channel region 2 days after printing showed an initial adherence of HUVECs to the inner surface of the printed channels and more clustering prior to sprouting (**Figure 5**a–d). However, with HU_hMSCs^{high}, an enhanced angiogenic patterning was observed and HUVECs seemed to directly elongate and form network junctions as well as forming sprouts advancing into the invasion region (Figure 5b,e). In both groups, hMSCs printed into the bulk material spread into the invasion region and migrated toward the HUVECs in the channel, but to a significant larger extent for HU_hMSCs^{high} (Figure 5a,b). In the invasion region, while a reduced number of HUVECs immigrated in the group HU_hMSCs^{low} (Figure 5e), an increased hMSC concentration (HU_hMSCs^{high}) resulted in an interconnected microvascular network formation (Figure 5f). These networks showed signs of anastomosis of the two vascular networks originating from two neighboring channels as early as 2 days after printing. At 10th day, especially for HU_hMSCs^{high}, a denser interaction of hMSCs wrapping around the microvascular structures was detected both in the channel (Figure 5i,j) and the invasion region (Figure 5m,n). hMSCs in the bulk migrated into the invasion region when printed in proximity to the invasion region (Figure 5o,p). In addition, the microvascular structures in HU_hMSCs^{high} showed a rather consistent diameter indicating an eventual maturation and lumen formation (Figure 5j,n). The wrapping behavior of MSCs, i.e., to reside in perivascular locations, confirms the active participation of the supporting cell type in vascular assembly as described before.[4,25,26] This close interaction and wrapping presumably provided a luminal stabilization and is an indication for maturation of the endothelial network.[4] Lumen formation was verified by an additional cross-sectional imaging with a confocal microscope (Figure S3, Supporting Information). Additional staining against alpha smooth muscle actin (α-SMA) of the group HU_hMSCs^{high} (Figure S4, Supporting Information) was performed. The presence of α-SMA and the co-alignment with the endothelial network are indicators for the ability of hMSCs to differentiate into perivascular cells and suggest vascular stabilization and maturation.[4,15,25,26] Interconnection/branching points of the microvascular network are illustrated additionally in 3D using the software Imaris (Bitplane) showing the open lumen and connection points from different angles (**Figure 6**).

2.4. hMSCs Induced a Concentration-Dependent Interconnected Vascular Network while hdFs Induced Longer and Highly Aligned Vascular Bundles

Besides different concentration of hMSCs, hdFs were utilized as supporting cell type to investigate possible differences due to biomechanical and biochemical interactions in the formation of vascular structures in vitro. The individual supporting cell types were printed in the bulk material and three different groups (HU_hMSCs^{low}, HU_hMSCs^{high}, and HU_hdFs) were analyzed for their capacity to form microvascular structures.

As described above, hMSC concentration altered the process of microvascular network formation, total vessel length, and the ability of HUVECs to invade the invasion region (**Figure 7**a,b). Comparing the setups with hMSCs and hdFs at equal concentration revealed a substantially reduced microvascular structure formation and only very little migration of HUVECs out of the channels when bioprinted with hdFs (compare Figure 7b,c). The orientation of HUVECs within the channels showed a progressively increasing arrangement of microvascular structures parallel to printed channels (0°) over time for all groups and was most pronounced in the case of HU_hdFs (Figure 7d).

As early as 2 days after printing, hMSCs and hdFs had migrated from the bulk material to the channels, presented by hMSC/hdF coverage in this region (Figure 7e, patterned bars). The cell coverage after 2 days also indicated that hdFs migrated faster into the channel than hMSCs, although HUVEC coverage was only approximately half as high when cultivated with hdFs. For the later time points, the population of hMSCs and HUVECs seemed to progressively increase. However,

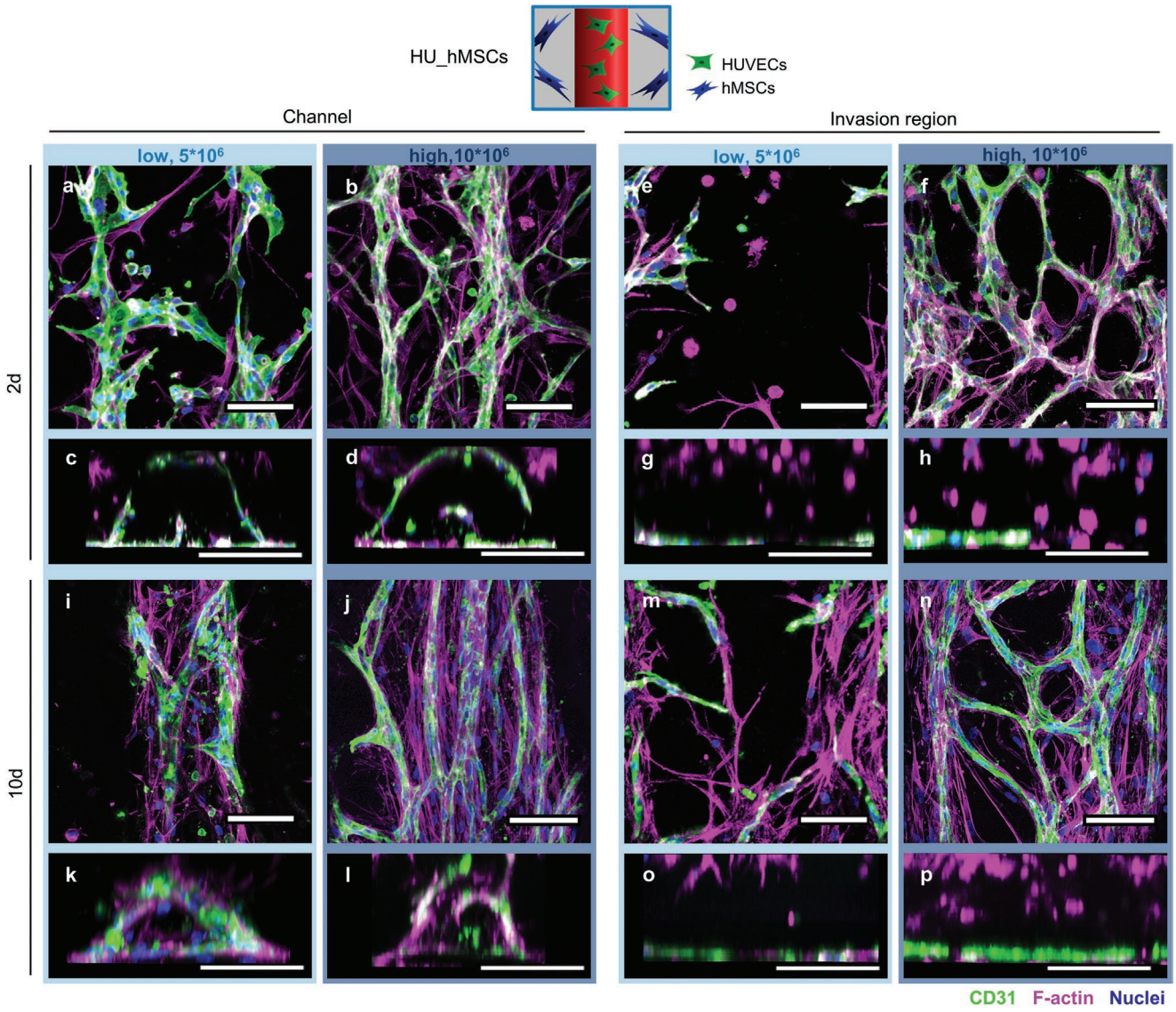

Figure 5. Cellular behavior of HUVECs (green) and hMSCs (magenta) printed locally separated from each other at different hMSC concentration (HU_hMSCs^{low}, light blue frame, and HU_hMSCs^{high}, dark blue frame). HUVECs were printed into the channel and hMSCs in bulk. a,b) Representative confocal images of the channel region 2 days post printing with a generally enhanced neovascularization for a higher hMSC concentration and corresponding c,d) front view reconstructions with Imaris (Bitplane). e,f) Representative confocal images of the invasion region after 2 days, showing (e) only little HUVECs immigrated from the channel in case of lower concentration of hMSCs but an already formed (f) premature, interconnected vascular network with hMSCs in proximity in case of higher hMSC concentration. g,h) Front view reconstructions of the invasion region after 2 days. i,j) Top view image 10 days post printing in the channel with microvascular structures surrounded by a network of hMSCs and corresponding k,l) front view reconstruction. m,n) Confocal images of the invasion region after 10 days. n) HU_hMSCs^{high} formed an interconnected microvascular network originating from neighboring channels. o,p) Front view reconstruction of the invasion region after 10 days showing no bulk penetration of microvascular structures. hMSCs in the bulk in proximity to invasion region seemed to have migrated into the invasion region. Scale bars: a,b,e,f,i,j,m,n) 50 µm, c,d,g,h,k,l,o,p) 200 µm. Samples were stained for CD31 (HUVECs, green), nuclei (blue) and F-actin (hMSCs and HUVECs, magenta).

although the complete channel area seemed to be covered with cells already at early time points for the group HU_hdFs, the ratio of HUVECs to hdFs increased with time, probably as a consequence of the development and maturation of the microvasculature within the channel. Overall, the highest HUVEC coverage was found in the group HU_hMSCs^{high}, in agreement with the more developed and interconnected microvascular structure (Figure 7b). The density and connectivity of the microvascular structure was the highest for the group HU_hMSCs^{high} (Figure 7f,g), although both HU_hMSCs^{low} and HU_hdFs showed remarkably similar VLD and BPD despite their spatial distribution across the channels (compare Figure 7a,c).

In the invasion region, a progressive cell migration and proliferation was observed for both supporting cell types (Figure 7h). HUVEC coverage also progressively increased for the groups with hMSCs as supporting cells. Similar as in the channel region, the highest HUVEC coverage was found in the group HU_hMSCs^{high}. However, HUVECs were barely present

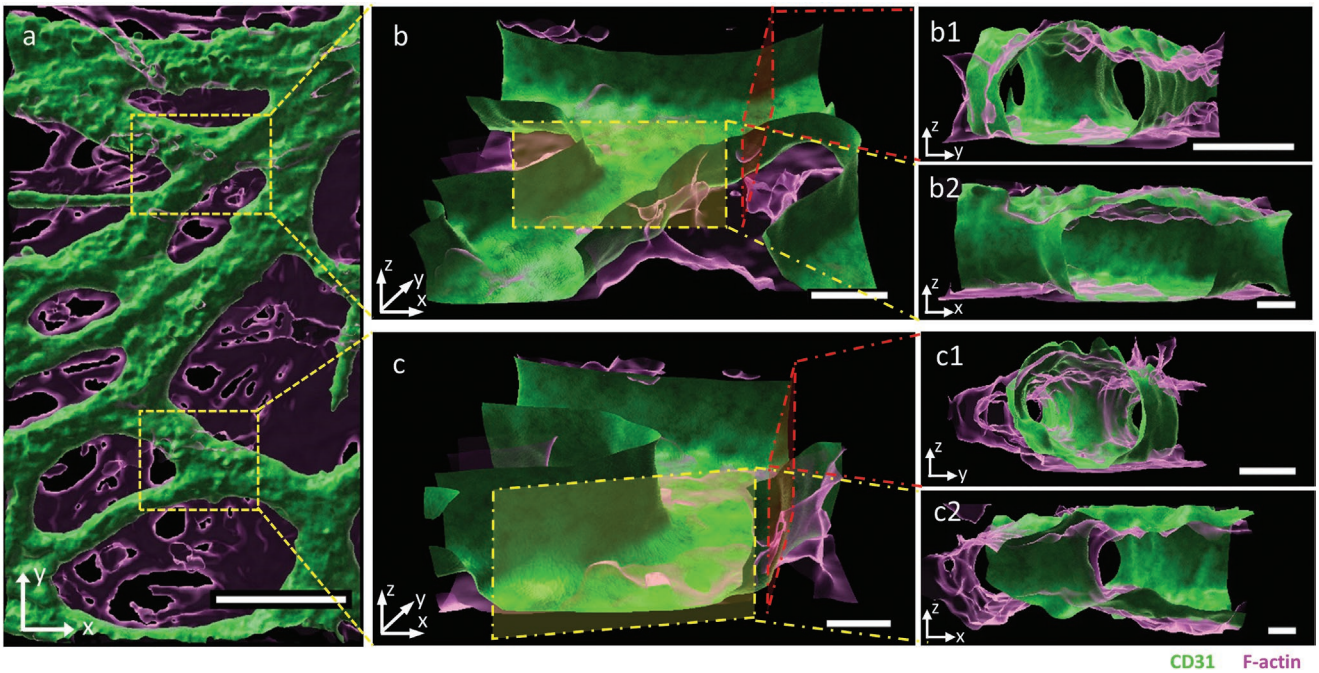

Figure 6. Confocal images of the interconnected vascular network in different angles. Vascular network was segmented using the surface function of the Imaris software (Bitplane). The CD31 signal represents the HUVECs/vascular structures (green) and the F-actin staining corresponds to the hMSCs (magenta). a) Overview image (scale bar: 50 µm) in top view (xy-plane) and b,c) two exemplary interconnection/branching points (position marked in subfigure a with yellow squares) (scale bars: 20 µm). The images show the vascular branching point in a tilted angle and sliced in z-direction showing the lumen of the vascular structure. (b1, 2 and c1, 2) Images were sliced in the front and lateral plane (position indicated with yellow and red plane) showing the open channel structure and the branching point in a zy-view.

in this area for the group HU_hdFs as it was mostly occupied by hdFs (Figure 7h, patterned bars). Consequently, VLD and BPD showed a striking different pattern in the group HU_hdFs compared to the channel region as the microvasculature was almost absent in the invasion region. The group HU_hMSCs^{high} again presented the highest density and connectivity (Figure 7i,j), resulting in even higher branching after 10 days when compared to the channel region (compare Figure 7g,j, 10d).

Altogether, the results indicate that hMSCs at a higher printing density induced a faster formation of microvascular structures and reveal a concentration-dependent vascular density and branching. In contrast, the ability of the cells to form angiogenic sprouts originating from the channels and expanding into the invasion region was limited when using hdFs as supporting cell type. Although the hdFs seemed to proliferate at a higher rate than HUVECs, and hence could have diminished the capacity of the latter to migrate toward the already populated invasion region, differences in the mechanical interaction between the two cell types and paracrine effects cannot be excluded as the microvascular structure is significantly different from that formed by a combination of hMSCs and HUVECs.

3. Discussion

With the aim to bioengineer distinct microvascular structures by combining a 3D multi-material bioprinting strategy and cellular self-organization, we developed a 3D-bioprinted vascularized construct with distinct compartments for microvascular formation: channels and invasion regions. These were realized using two distinct biocompatible inks: the bulk material was printed using GelMA while the channels were realized with an enzymatically degradable sacrificial photoink (HAMA) (Figure 1). We previously introduced a sacrificial material system to generate open channels using HAMA bioink, which was shown to degrade within a few hours while presenting high viability for the embedded cells (Figure 1h).[21] Since it has been shown that the local mechanical environment affects cell behavior aspects like spreading, migration, proliferation, and differentiation,[27] the E-moduli of the materials were selected in a low range (1–4 kPa) to mimic the stiffness of natural soft tissue such as brain, spleen, skin, and muscles (E ≈ 0.2–15 kPa)[28] and their stress relaxation behavior. The E-modulus can be adapted by the degree of functionalization (DoF), the concentration of GelMA/HAMA and photoinitiator as well as the exposure time. Beyond stiffness, the stress relaxation behavior of the bioprinted constructs was similar to soft tissues such as bone marrow coagulate or fracture hematoma, thus ensuring cell spreading and migration within the construct.[23] However, information about how to tune the stress relaxation of bioprinted hydrogels remains scarce. In addition, the DoF of the material itself also influences the behavior of encapsulated cells and vascular network formation.[4,29] The mean methacrylation degree of GelMA of 59.8 ± 9.6% (mean ± SD) was in the range of the reported DoF for optimal pore size and stiffness for cell viability, growth, migration, and spreading as well as

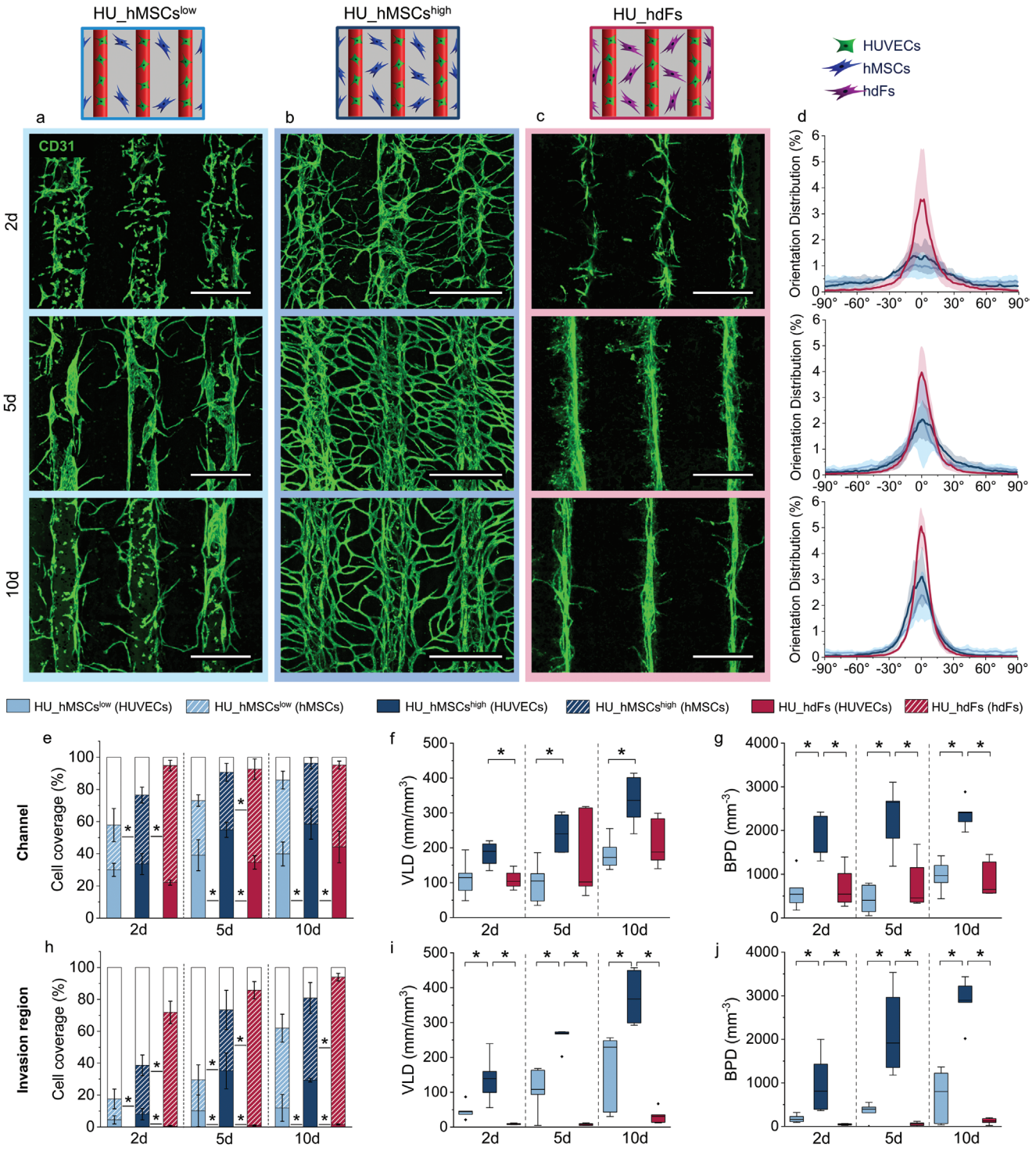

Figure 7. Regulation of microvascular structure formation by altering cell placement, concentration of hMSCs in the bulk, and cell type. Direct comparison of the group a) HU_hMSCs^{low} (light blue), b) HU_hMSCs^{high} (dark blue), and c) HU_hdFs (magenta) visualized by maximum projection of representative confocal images stained for CD31 (green) for 2, 5, and 10 days post printing. Scale bars: 500 µm. d) Cell orientation analysis within the channel of 2, 5, and 10 days post printing (from top to bottom). Cell coverage (HUVEC coverage = full bar, hMSC/hdF coverage = patterned bar, empty/uncovered area = white bar)), VLD and BPD of the vascular structures in the e–g) channel and in the h–j) invasion region for 2, 5, and 10 days. Statistical significance via Mann–Whitney test (two sided), $^{*}p < 0.05$, $n = 5$.

establishing cell-cell contacts.[29] The DoF for HAMA was considerably lower due to its role as sacrificial ink, as it has been shown that the speed of enzymatic degradation is inversely correlated with the DoF of a material.[29] Consequently, the bioink

optimization of the construct showed high viability ratios independently of the type of bioink or cell concentration, highlighting the suitability of the system as a platform for analyzing complex cellular processes.

The combination of these two bioinks with the layer-by-layer printing approach resulted in invasion regions between the channels, at the interface between the base and top GelMA layer (Figure 2). The invasion region, due to its favorable conditions for cell migration, provoked particular interest as it enabled the possibility to analyze the formation of vascular structures in restricted compartments as well as the effect of cell positioning on cellular interactions.

Bioprinting of ECs without a supporting cell type (Group HU-mono) led to the formation of an endothelial lining of nearly the complete inner surface of the printed channels within 10 days but was insufficient to create microvasculature structures (Figure 2d). The endothelialized channels presented endothelial cell-cell junctions as visualized by staining against CD31 and vascular endothelial cadherin (VE-cadherin) (Figure 2c–j), which function as regulators of vascular permeability.[30,31] The presence of both markers indicated an important aspect of vascular functionality, i.e., the endothelial barrier. Moreover, the endothelialized bioprinted channel with a size of ≈0.2 mm in diameter and 5.5 mm in length presented an open lumen (Figure 2f) for possible perfusion, as shown in our previous study.[21] This could be of special relevance for the creation of endothelialized fluidic channels to support the viability of large constructs for tissue engineering applications.[12,32] Our findings are thus in agreement with other studies where ECs cultivated in mono-culture formed cell-cell junctions and no tube-like microstructures.[19,33,34] As ECs in mono-culture cannot generate the pro-angiogenic factors for the formation of microcapillaries themselves,[19,33,34] we decided to include a supporting cell type.

Multiple studies have shown that a co-cultivation of ECs with a second, supporting cell type like hMSCs, fibroblasts or osteoblasts, is essential for vascular self-assembly, the formation of capillary-like networks and angiogenesis in vitro, as these cells are capable of producing required proangiogenic factors for the formation and maturation of vasculature.[4,11,14–16,19,33] In our studies, by controlling the spatial placement of the supporting cell type and the ECs, we were able to alter the impact of cell-cell contact and potentially paracrine signaling, consequently modulating the cellular self-assembly processes and the patterning of the forming microvascular structures.[24] These structures showed signs of stabilization and maturation by means of perivascular investment and hMSCs wrapping around microvascular structures as well as expression of α-SMA (Figure S4, Supporting Information).[4,15,25,26] The combination of both cell types in the channels (group HU+hMSCs) showed endothelial elongation and de novo network formation without prior endothelial clustering, which is usually exhibited prior to sprouting.[6] This approach led to the formation of highly oriented microvascular structures via initial neovascularization with only little migration of HUVECs and microvascular structures into the invasion regions and without penetrating the bulk (Figure 3). This is in accordance with previous findings demonstrating that HUVECs remain within printed regions for 24 h when in co-culture with hMSCs, reducing EC migration by the presence of the supporting cell type.[35] The migratory activity of HUVECs has been shown to decrease when exposed to conditioned media of HUVECs and MSCs cultivated in close proximity, and it was correlated to an increase in Ang-1 and VE-cadherin expression demonstrating angiogenic stabilization.[24] This is in agreement with the fact that the HUVECs coverage remained fairly constant over time in the group HU+hMSCs, indicating a process of cellular rearrangement rather than a strong proliferation. This might be explained by the immediate contact of the two cell types in the channel that might also prevent the invasion of microvascular structures out of the channel into the invasion region.

On the other hand, our study showed that separating HUVECs and hMSCs resulted in a strong migration of HUVECs and microvascular structures from the channels into the invasion region and demonstrated an hMSC dosage dependency on the migration capacity of HUVECs (Figures 5 and 6). The effect of distance between cell populations on their crosstalk has been recently studied using a 2D proliferation, migration, and tube formation assay supplemented with conditioned medium of HUVECs and MSCs cultivated at different distances.[24] Results showed an increasing HUVEC migratory activity and tube length for increasing distance between HUVECS and MSCs. HUVECs grown farther apart from MSCs presented stronger migration and proliferation, and an increase in upregulation of vascular endothelial growth factor (VEGF) and fibroblast growth factor-2 (FGF-2). On the other hand, HUVECs cultivated closer to MSCs demonstrated an increase in Ang-1 and VE-cadherin expression. While the mentioned study investigated HUVEC migration and tube formation indirectly in a 2D environment using conditioned medium, our results using a 3D-bioprinted construct seem to validate these findings, as separating the two cell types resulted in a strong migration of vascular structures into the invasion region. In addition, the migration seemed to promote the rapid formation of longer microvascular structures in the invasion region as well as stronger sprouting compared to the channel region and when printed together (compare Figures 4b,f–i and 6b,f,g,i,j). This process of invasion was purely orchestrated by angiogenesis of vascular structures out of the channel as no HUVECs were printed in this region, while, in the channel, a process of de novo vascular formation and angiogenesis was observed for both conditions (compare Figures 3 and 5). Moreover, the separation of the two cell types suggest an effect of increased HUVEC proliferation, since HUVEC coverage was constant for the group HU+hMSCs but increased for the group HU_hMSCs over time (compare Figures 4d,e and 6e,h). Remarkably, separating the two cell types seemed to have triggered the process of anastomosis, connecting microvascular structures originating from different channels, indicating that the invasion region between the channels placed 400 µm apart allows paracrine interactions between neighboring channels (Figure 5f,n).[24]

We were able to show that besides cell placement, also the dosage of the supporting cell type printed into the bulk material influences the self-assembly process of microvascular structures. The change in hMSC concentration seemed to change the cellular interaction between the two cell types. Printing a low concentration of hMSCs in the bulk led to HUVECs adhering

to the inner surface of the printed channels, forming multicellular endothelial clusters and then sprouting in direction of the hMSCs (Figure 5, HU_hMSCs^{low}). This process seems reminiscent of the in vivo neovascular morphogenesis process, which consists of vasculogenesis followed by angiogenesis.[6] In contrast, in the group HU_hMSCs^{high} HUVECs showed signs of de novo network formation with a direct endothelial elongation and sprouting, although without the initial occurrence of endothelial clusters (Figure 5, HU_hMSCs^{high}).[6]

In addition to MSCs,[4,15,18,19] fibroblasts[5,11,14–16] can also support the formation of vascular structures. Gene expression profiles and cell surface markers of hMSCs and fibroblasts have been shown to be similar, but only hMSCs demonstrate multilineage differentiation and colony-forming potential.[36,37] MSCs and fibroblasts have been used to induce regeneration in multiple constellations: human fibroblast allografts were used as treatment for diabetic foot ulcers or in restoring skin following severe burn injuries;[38,39] MSCs were used to induce bone defect healing or for ischemic heart diseases[39,40] or skeletal muscle regeneration.[41] However, fibroblasts are easier to be harvested and are known to play a critical role in wound healing and ECM formation, e.g., by depositing ECM surrounding nascent blood vessels, fibronectin, and collagen.[6,38,42] Due to the exhibited differences and the scarcity of studies with a direct comparison between MSCs and fibroblasts in respect to influencing endothelial cells in their vascular formation in 3D constructs in vitro, we included this comparison in our study. While hMSCs strongly promoted sprouting not only in the channel, but also in the invasion region, hdFs caused limited HUVEC migration and angiogenesis, leading to the formation of highly oriented microvascular structures with little branching and present exclusively within the channels (compare Figure 6b,c). The strong difference in the microvasculature pattern may be explained by the greater proliferation and migration potential of hdFs compared to those of hMSCs.[38,43,44] Consequently, the vascular structures might have been repressed in the channels by high numbers of hdFs already having migrated into the vascular compartments as early as 2 days after printing (Figure 6c,e,h). However, a stronger HUVEC invasion and higher degree of vascularization could be expected as the concentration of hdFs is reduced.

Altogether, geometrical constrains in combination with the control of cell placement in 3D, cell concentration and cell type allowed to regulate the pattern and self-assembly of micro- and macro-vascular structures. Harnessing the principles of cellular self-organization allowed to generate constructs with distinctly vascularized compartments beyond pre-engineering details of 3D microvascular complexity. Our data suggest that such bioengineering approach opens so far unexploited possibilities to steer and design vascular self-assembly within a construct, presenting the unique capability to create macro- or microvascular networks using the same construct design by choosing different cellular configurations.

The endothelialized channels may serve as source of perfusion resembling larger vascular structures, while the microvascular structures ensure sufficient supply throughout the entire construct, solving the limitations of oxygen diffusion (100–200 µm).[14] This could be of special interest when considering vascular organization of different tissues and organs, e.g., a parallel alignment of vessels to the muscle fiber in comparison to a dense, intricate organization in liver.[8,11] Additionally, our design allows the fabrication of different compartments, consisting of adjacent vascular and avascular regions like in the eye (vascular uvea and retina and avascular cornea and lens)[45] and skin (vascular dermis and avascular epithelial layer).[46] These capabilities of the system would also allow the development of disease models, e.g., for avascular necrosis in bone.[47] Therefore, controlling the patterning and restricting vasculature to certain compartments can be regarded beneficial not only for in vitro screening systems, vascular physiology studies or for developing organ-on-a-chip models,[48] but also for the design of future tissue engineering approaches with precise microvasculature to potentially enhance regeneration.

4. Conclusion

The presented bioengineering approach of a bioprinted, patterned vascular construct allows the detailed investigation and control of neovascularization and angiogenesis. This system allows the generation of macrovascular channels by an endothelial lining as well as the formation of controllable microvascular structures via cellular self-assembly processes through adjustment of the bioprinting set-up, i.e., by altering cell location, entity, and dosage. The fast generation of these well-defined vascular patterns were either exclusively oriented along the channels or forming strongly interconnected microvascular networks. The formation of vascular structures could be induced and regulated by varying the supporting cell type and placement. Incorporated cells demonstrated the ability to form microvascular structures with lumen within a few days of cultivation and showed signs of stabilization and maturation, as well as forming interconnected vascular networks by angiogenesis and anastomosis. Together, we were able to control the amount, orientation, length, and branching behavior of the forming vascular structures by engineering different spatial arrangement of cells to control cell-cell interaction, migration, and proliferation allowing us to investigate how cell type and spatial configuration affect the self-assembly of macro- and micro-vascular structures. This innovative strategy of combining the power of cellular self-assembly with a spatial control of the vessel formation allows the development of distinct yet precise vascularization. The formation of vascular structures via self-organization should be considered superior over the artificial production of vascular structures considering functionality, complexity, and adaptability for the potential use in tissue engineering and regenerative therapies.[5,12,49]

5. Experimental Section

Cell Isolation and Culture: HUVECs (Lonza) were cultivated in complete endothelial cell growth medium 2 (ECGM-2, PromoCell) supplemented with 1% v/v penicillin/streptomycin (P/S; Biochrom AG). Experiments were performed at passages 5 – 6. hMSCs were isolated from the bone marrow of donors undergoing total hip joint replacement surgeries.[50] hMSCs were cultured in medium consisting of Dulbecco's modified Eagle's medium (DMEM) – low glucose (Sigma–Aldrich) supplemented with 10% v/v fetal bovine serum (FBS, Sigma–Aldrich),

1% v/v P/S, and 1 % v/v GlutaMAX™ (Gibco). Experiments were performed at passage 5. hdFs were isolated from skin biopsies by outgrowth culture. hdFs were cultured in medium containing DMEM – high glucose (Gibco) supplemented with 10% v/v FBS, 1% v/v P/S, and 1% v/v non-essential amino acids (Bio&SELL). Experiments with hdFs were performed at passage 7. All cells were cultured in standard cell culture conditions of 37 °C with 5% CO_2 and 100 % humidity. Medium exchange was performed every 3 to 4 days, and cells were passaged/harvested before reaching confluency. Ethical approval for human dermal fibroblasts (ethical approval number EA1/359/13) and human mesenchymal stromal cells (ethical approval number EA4/067/19) was obtained from the ethics committee of Charité – Universitätsmedizin Berlin and written informed consent from the donors was given.

Bioink Synthesis: Synthesis was performed by Cellbricks GmbH. Two bioinks were used in this printing concept: GelMA served as bulk material and HAMA as an enzymatically degradable sacrificial bioink. GelMA was synthesized from gelatin (300 bloom) from porcine skin (Sigma–Aldrich) by methacrylation as described previously.[51,52] Briefly, 10% w/v gelatin was solved in phosphate-buffered saline (PBS, Thermo Fisher) and temperature was adjusted to 50 °C. Methacrylic anhydride (Sigma–Aldrich, 0.1 mL g^{-1} gelatin) was added gradually and stirred for 3 h. After adjusting the pH to 7.4, the solution was dialyzed with a 12–14 kDa cut-off membrane against distilled water for 4 days. To synthesize HAMA, hyaluronic acid from *Streptococcus Equi* (molecular weight >1 MDa, Alfa Aesar) was autoclaved to reduce chain length. The synthesis was carried out as previously reported [21] using a modified protocol.[53] Briefly, hyaluronic acid (Alfa Aesar) was dissolved in Milli-Q® water (1% w/v solution), which was adjusted to pH 9.0. A solution of methacrylic anhydride (2.0 mL g^{-1} HA) dissolved in 5 mL dimethyl sulfoxide (VWR) was added and stirred for 24 h at room temperature, followed by a dialysis against Milli-Q® water with a 12–14 kDa cut-off membrane. Both bioinks were subsequently lyophilized (–60 °C, 1 mbar) to obtain a long-lasting GelMA and HAMA stock. Lithium phenyl-2,4,6-trimethylbenzoyl phosphinate (LAP) was synthesized as described elsewhere and served as photoinitiator.[54,55]

Mechanical Testing: Unconfined compression tests were performed by Cellbricks GmbH using a texture analyser (2.5 kN RetroLine, Zwick Roell GmbH) to determine the bulk elastic moduli (E-modulus) of printed hydrogel discs of 7% (w/v) GelMA and 1.5% (w/v) HAMA.[21] Values were presented as mean and SD of three discs, each consisting of a data set of five repeated and averaged measurements. Hydrogel disc diameters were measured prior to the compression tests with a digital microscope and corresponding analysis software. Stress–stain curves of each material were recorded and the compressive Young´s modulus was calculated in the slopes between 0% and 10% strain. A nanoindentation device (Piuma Inc., Optics11) was used to measure the local E-modulus of printed constructs in the dimensions $4.0 \times 5.5 \times 0.8$ mm (width x length x height) with 7% (w/v) GelMA similar to the constructs used in the in vitro experiments. The indentation tips (radius 46 µm) covered different positions of three printed construct (at least 12 measurements). A Poisson ratio of 0.5 was assumed for the indentation model determining an effective E-modulus that is presented as the mean and SD over each construct. Additionally, the stress relaxation behavior of one GelMA construct was exemplarily measured with the nanoindentation device by adding a 30 s dwell after indentation. The stress relaxation time $\tau_{1/2}$ was defined as the time interval between the maximum force (normalized) and the time needed to drop to half of the equilibrium force while maintaining constant indentation. One exemplary construct was tested at six different positions and values were averaged.

Nuclear magnetic resonance (NMR): The DoF of synthesized GelMA and HAMA was measured by Cellbricks GmbH using a 1H NMR spectrometer at 500 MHz. The DoF of GelMA was calculated with the fraction of functionalized lysine residues, the DoF of HAMA[21] by the number of (meth)acrylic groups per repetitive disaccharide unit. Three samples per material were tested.

Conceptual Design and Bioprinting Process: A 3D-printed structure was designed using Rhinoceros 6 (Robert McNeel & Associates) with a volume of $4.0 \times 5.5 \times 0.8$ mm (width x length x height). It was digitally sliced to three distinct and consecutively printed layers of variable height (Figure 1a). The base layer consisted of GelMA, the second contained five parallel channels consisting of the sacrificial bioink HAMA, and the third acted as a top covering layer of GelMA. The five parallel channels were designed with a cross-sectional size of 0.2×0.2 mm and a length of 5.5 mm each and were oriented along the long axis of the cuboid with a distance between the channels of 0.4 mm (Figure 1c). The final design was transferred to the bioprinter (Cellbricks GmbH) and fabricated using a multi-material projection-based stereolithography process at 50 µm per pixel resolution.[21] The lyophilized stock bioink materials were dissolved in PBS to the desired concentration of the bioink and 0.1% w/v LAP was added. The permanent structures (i.e., the bulk) were printed with 7% w/v GelMA, the enzymatically degradable channels were printed using 1.5% w/v HAMA. When necessary for the corresponding layers, cells were suspended into the pre-warmed ink directly prior to bioprinting. Four groups with different cell placements were created and analyzed without changing the construct layout (Figure 1d): A) Group HU-mono: Only HUVECs printed in channels with a concentration of 20×10^6 cells mL^{-1}. No cells printed in the surrounding GelMA bulk. B) Group HU+hMSCs: Jointly HUVECs and hMSCs printed in a ratio of 1:1 in channels with a total concentration of 20×10^6 cells mL^{-1}. No cells printed in the surrounding GelMA bulk. C) Group HU_hMSCs: HUVECs printed in channels with a concentration of 20×10^6 cells mL^{-1}. hMSCs printed in the surrounding GelMA bulk with either a concentration of 5×10^6 (HU_hMSCs^{low}) or 10×10^6 (HU_hMSCs^{high}) cells mL^{-1}. D) Group HU_hdFs: HUVECs printed in channels with a concentration of 20×10^6 cells mL^{-1}. hdFs printed in the surrounding GelMA bulk with a concentration of 10×10^6 cells mL^{-1}.

Bioprint Cultivation: After printing, constructs were transferred to a 24-well plate and cultivated in 500 µL ECGM-2 supplemented with hyaluronidase (Hase, 75 U mL^{-1}, STEMCELL Technologies) in each well. Adding the enzyme caused the degradation of the sacrificial ink (HAMA) defining the channels and allowed the release of the entrapped cells within hours.[21] The following day a medium exchange with 700 µl ECGM-2 and 1% v/v P/S was performed. Constructs were further cultivated up to 10 days performing a medium exchange every second day.

Bioprinting Fidelity: Length and width of printed constructs as well as the width of the printed channels were measured using a digital microscope (BZ-9000, Keyence) to assess printing fidelity. Each dimension was measured at three different positions and averaged over the sample. The height of the channels was measured with Imaris (Bitplane) in a 3D representation. The five channels of the construct were measured, and the values averaged. At least 11 constructs of four independent experiments were analyzed and presented as the mean and SD. The absolute error in µm was calculated by subtracting the measured mean dimensions from the designed CAD dimension. The relative error was calculated as the percentage of the absolute error to the designed dimensions.

Cell Viability Assay: The viability of cells after the printing process was tested in 7% (w/v) GelMA and 1.5% (w/v) HAMA[21] for the different cell types at the corresponding cell concentrations. HUVECs were solved at a concentration of 20×10^6 cell mL^{-1} HAMA and subsequently printed to discs of 3 mm diameter and 1 mm height. In case, HAMA was not enzymatically degraded a live dead staining with Hoechst33342 (Sigma–Aldrich) and CellTox™ Green (Promega) in normal incubation conditions was performed on the cells encapsulated in the hydrogel 20 h after printing ($n = 4$). Images were recorded using a digital microscope (BZ-9000, Keyence or BZ-X810, Keyence) in a total depth of 250 µm (in the central region of the print) and the scans digitally stitched. Since the HAMA was used as a sacrificial ink to produce channels a viability test with the addition of the enzyme hyaluronidase (Hase, 75 U mL^{-1}) was performed. The printed discs were degraded, the HUVECs released and collected in the medium supernatant. An automated live–dead cell count (NucleoCounter® NC-200, ChemoMetic) was performed and the viability calculated ($n = 4$).[21] In addition, the viability of hMSCs (5×10^6 and 10×10^6 cell mL^{-1}) and hdFs (10×10^6 cells mL^{-1}) was tested in 7% (w/v) GelMA. Constructs printed similar to the vascular sheets for

the later in vitro experiments with the dimensions of 4.0 × 5.5 × 0.8 mm (width x length x height) were analyzed following the same procedure as above using Hoechst33342 and CellTox™ Green as live–dead staining within 48 h after printing. Each sample was imaged twice and averaged. Data sets were presented as the mean and SD over four samples.

Fixation and Fluorescent Staining: The constructs were fixed after 2, 5, or 10 days of cultivation in 4% paraformaldehyde for 1 h at room temperature and stored in PBS at 4 °C. Fluorescent staining was performed for F-actin (phalloidin-Atto 550, Sigma–Aldrich, 1:400 dilution) to visualize the cytoskeleton of cells, and nuclei (DRAQ5™, BioLegend, 1:1000 dilution or DAPI, Invitrogen, 1:1000 dilution). The following primary antibodies were used: anti-CD31 (HEC7, Abcam, 1:200 dilution), anti-VE-Cadherin (Cell Signaling Technology, 1:600 dilution), anti-α-SMA (Cell Signaling Technology, 1:200 dilution), anti-laminin alpha 4/LAMA4 antibody (3H2, Abcam, 1:50 dilution). As secondary antibodies Alexa Fluor 488 goat anti-mouse, (1:400 dilution), Alexa Fluor 488 donkey anti-rabbit (1:400 dilution), F(ab')2-goat anti-mouse Alexa Fluor 488 (1:1000 dilution), Alexa Fluor Plus 647 goat anti-mouse (1:400 dilution), and Alexa Fluor 647 donkey anti-rabbit (1:400 dilution) were purchased from Invitrogen.

Confocal Imaging: Confocal images were taken with a Leica TCS SP5 II confocal laser scanning microscope (Leica Microsystems GmbH). The microscope was equipped with a MaiTai HP multiphoton laser and a 25x and 40x water immersion objective for tile scans or single spots, respectively. Tile scan image stacks were recorded in the central region of the construct for the complete depth of the printed channels at 512 × 512 px for each recorded image of one tile scan, resulting in a voxel size of 620 × 620 × 6 µm (width x length x depth) and a total minimum depth of 200 µm. Image stacks of single spots were recorded with the 40x immersion objective at a resolution of 1024 × 1024 px, resulting in a voxel size of 388 × 388 × 1.5 µm.

Postprocessing and Quantitative Analysis: Analysis of orientation distribution, cell coverage, the VLD, and BPD was conducted on tile scans by manual selection of channels and intermediate spaces between two channels, here referred to as invasion region (Figure 2a). To exclude edge effects, only 50 % of the total invasion region corresponding to the middle section was analyzed. This way, effects adjacent to the channels were excluded to ensure no influence of the channels on the outcome of the analysis. Regions close to the edges of the overall construct were also excluded from analysis. Each data point represents the mean of each construct, printed with five channels and four invasion regions. Each data set represents at least four printed constructs. The orientation distribution of the forming microvascular structures (CD31 signal) was quantified in the different regions using the maximum intensity projections of acquired image stacks with the plugin OrientationJ Distribution [56] developed for Fiji.[57] Only the central section (half of the total width) of the channel area as well as the invasion area were selected as ROIs to avoid edge effects. The percentage of orientation distribution was shown in a range of –90°–+90°, where 0° represented an orientation parallel to the printed channel structures (Figure 4c, top). Total area covered by HUVECs (CD31 signal) and supporting cells (visualized by phalloidin) were quantified using a custom-made macro including Vessel Analysis Plugin [58] for Fiji.[57] hMSC and hdF coverage (patterned bar) was estimated by subtracting HUVEC coverage (CD31 signal, full bar) from total cell coverage (phalloidin signal) (Figure 4d,e). Data were presented as percentage of area covered by cells over the total available area (cell area/total area). The empty area, which was not covered by cells was presented as white bar. Orientation distribution and coverage measurements were performed on the maximum intensity projection of the ROIs of the channel and invasion regions. Subsequently, VLD and BPD were analyzed in 3D using the Software Imaris (Bitplane). The FilamentTracer function was applied to the generated ROIs dividing between channel and invasion region. The obtained results were presented normalized to the volume of the channels or invasion regions.

Statistical Analysis: Orientation distribution plots were shown as xy-plots representing the mean value and standard deviation for all analyzed samples. Bar charts presented the mean standard deviation for the constructs. Box plots were defined by the 25th and 75th percentiles and the whiskers by the 5th and 95th percentiles. The median value was indicated as a horizontal line and outliers as rhombs outside the box. All statistical analyses were performed with OriginPro 2021b (OriginLab Corp.) using a two-sided Mann–Whitney-U statistical test to assess significance levels. A value of $p < 0.05$ was considered significant. At least two independent experiments per group were conducted with a sample number of four to five per group.

Supporting Information

Supporting Information is available from the Wiley Online Library or from the author.

Acknowledgements

I.O. and A.T. contributed equally to this work. The authors thank Dr. Sven Geißler and Dr. Simon Reinke (Core Unit "Cell Harvesting" of the Berlin Institute of Health Centre for Regenerative Therapies) for isolating hMSCs and providing human skin for hdFs isolation. This work was partially funded by grants from the German Research Foundation within the FOR 2165 "Regeneration in Aged" and the CRC 1444.

Open access funding enabled and organized by Projekt DEAL.

Conflict of Interest

The authors declare no conflict of interest.

Data Availability Statement

The data that support the findings of this study are available from the corresponding author upon reasonable request.

Keywords

bioprinting, controllable microvascular patterning, stereolithography, tissue engineering, vasculature

Received: July 20, 2022
Revised: September 22, 2022
Published online: November 2, 2022

[1] S. K. Ramasamy, A. P. Kusumbe, R. H. Adams, *Trends Cell Biol.* **2015**, *25*, 148.
[2] C. G. Fonseca, P. Barbacena, C. A. Franco, *Vasc. Biol.* **2020**, *2*, H29.
[3] J. S. Miller, K. R. Stevens, M. T. Yang, B. M. Baker, D.-H. T. Nguyen, D. M. Cohen, E. Toro, A. A. Chen, P. A. Galie, X. Yu, R. Chaturvedi, S. N. Bhatia, C. S. Chen, *Nat. Mater.* **2012**, *11*, 768.
[4] Y. Chen, R. Lin, H. Qi, Y. Yang, H. Bae, J. M. Melero-Martin, A. Khademhosseini, *Adv. Funct. Mater.* **2012**, *22*, 2027.
[5] D. B. Kolesky, R. L. Truby, A. S. Gladman, T. A. Busbee, K. A. Homan, J. A. Lewis, *Adv. Mater.* **2014**, *26*, 3124.
[6] Y. J. Blinder, A. Freiman, N. Raindel, D. J. Mooney, S. Levenberg, *Sci. Rep.* **2016**, *5*, 17840.
[7] C. Tomasina, T. Bodet, C. Mota, L. Moroni, S. Camarero-Espinosa, *Materials (Basel)* **2019**, *12*, 2701.
[8] B. A. Corliss, C. Mathews, R. Doty, G. Rohde, S. M. Peirce, *Microcirculation* **2019**, *26*, e12520.

[9] R. S. Udan, J. C. Culver, M. E. Dickinson, *W. Interdiscip. Rev. Dev. Biol.* **2013**, *2*, 327.
[10] J. D. Baranski, R. R. Chaturvedi, K. R. Stevens, J. Eyckmans, B. Carvalho, R. D. Solorzano, M. T. Yang, J. S. Miller, S. N. Bhatia, C. S. Chen, *Proc. Natl. Acad. Sci. USA* **2013**, *110*, 7586.
[11] D. Rosenfeld, S. Landau, Y. Shandalov, N. Raindel, A. Freiman, E. Shor, Y. Blinder, H. H. Vandenburgh, D. J. Mooney, S. Levenberg, *Proc. Natl. Acad. Sci. USA* **2016**, *113*, 3215.
[12] L. E. Bertassoni, M. Cecconi, V. Manoharan, M. Nikkhah, J. Hjortnaes, A. L. Cristino, G. Barabaschi, D. Demarchi, M. R. Dokmeci, Y. Yang, A. Khademhosseini, *Lab Chip* **2014**, *14*, 2202.
[13] D. H. T. Nguyen, S. C. Stapleton, M. T. Yang, S. S. Cha, C. K. Choi, P. A. Galie, C. S. Chen, *Proc. Natl. Acad. Sci. USA* **2013**, *110*, 6712.
[14] V. K. Lee, A. M. Lanzi, H. Ngo, S.-S. Yoo, P. A. Vincent, G. Dai, *Cell. Mol. Bioeng.* **2014**, *7*, 460.
[15] A. Freiman, Y. Shandalov, D. Rozenfeld, E. Shor, S. Segal, D. Ben-David, S. Meretzki, D. Egozi, S. Levenberg, *Stem Cell Res. Ther.* **2016**, *7*, 5.
[16] X. Chen, A. S. Aledia, S. A. Popson, L. Him, C. C. W. Hughes, S. C. George, *Tissue Eng., Part A* **2010**, *16*, 585.
[17] Y. Cao, Y. Gong, L. Liu, Y. Zhou, X. Fang, C. Zhang, Y. Li, J. Li, *J. Appl. Toxicol.* **2017**, *37*, 1359.
[18] O. Tsigkou, I. Pomerantseva, J. A. Spencer, P. A. Redondo, A. R. Hart, E. O'Doherty, Y. Lin, C. C. Friedrich, L. Daheron, C. P. Lin, C. A. Sundback, J. P. Vacanti, C. Neville, *Proc. Natl. Acad. Sci. USA* **2010**, *107*, 3311.
[19] H. Li, R. Daculsi, M. Grellier, R. Bareille, C. Bourget, M. Remy, J. Amedee, *PLoS One* **2011**, *6(2)*, e16767.
[20] J. C. Culver, J. C. Hoffmann, R. A. Poché, J. H. Slater, J. L. West, M. E. Dickinson, *Adv. Mater.* **2012**, *24*, 2344.
[21] A. Thomas, I. Orellano, T. Lam, B. Noichl, M. A. Geiger, A. K. Amler, A. E. Kreuder, C. Palmer, G. Duda, R. Lauster, L. Kloke, *Acta Biomater.* **2020**, *117*, 121.
[22] W. R. Legant, A. Pathak, M. T. Yang, V. S. Deshpande, R. M. McMeeking, C. S. Chen, *Proc. Natl. Acad. Sci. USA* **2009**, *106*, 10097.
[23] O. Chaudhuri, L. Gu, D. Klumpers, M. Darnell, S. A. Bencherif, J. C. Weaver, N. Huebsch, H. Lee, E. Lippens, G. N. Duda, D. J. Mooney, *Nat. Mater.* **2016**, *15*, 326.
[24] C. Piard, A. Jeyaram, Y. Liu, J. Caccamese, S. M. Jay, Y. Chen, *Biomaterials* **2019**, *222*, 119423.
[25] J. M. Melero-Martin, M. E. De Obaldia, S.-Y. Kang, Z. A. Khan, L. Yuan, P. Oettgen, J. Bischoff, *Circ. Res.* **2008**, *103*, 194.
[26] S. Trkov, G. Eng, R. D. Liddo, P. P. Parnigotto, G. Vunjak-novakovic, *J. Tissue Eng. Regener. Med.* **2010**, *4*, 205.
[27] C. C. DuFort, M. J. Paszek, V. M. Weaver, *Nat. Rev. Mol. Cell Biol.* **2011**, *12*, 308.
[28] D. E. Discher, D. J. Mooney, P. W. Zandstra, *Growth (Lakeland)* **2010**, *324*, 1673.
[29] I. Pepelanova, K. Kruppa, T. Scheper, A. Lavrentieva, *Bioengineering* **2018**, *5*, 55.
[30] P. Lertkiatmongkol, D. Liao, H. Mei, Y. Hu, P. J. Newman, *Curr. Opin. Hematol.* **2016**, *23*, 253.
[31] D. Vestweber, *Arterioscler. Thromb. Vasc. Biol.* **2008**, *28*, 223.
[32] V. K. Lee, D. Y. Kim, H. Ngo, Y. Lee, L. Seo, S. S. Yoo, P. A. Vincent, G. Dai, *Biomaterials* **2014**, *35*, 8092.
[33] R. Gauvin, Y.-C. Chen, J. W. Lee, P. Soman, P. Zorlutuna, J. W. Nichol, H. Bae, S. Chen, A. Khademhosseini, *Biomaterials* **2012**, *33*, 3824.
[34] R. E. Unger, E. Dohle, C. J. Kirkpatrick, *Adv. Drug Delivery Rev.* **2015**, *94*, 116.
[35] J. M. Bourget, O. Kérourédan, M. Medina, M. Rémy, N. B. Thébaud, R. Bareille, O. Chassande, J. Amédeé, S. Catros, R. Devillard, *Biomed Res. Int.* **2016**, 3569843.
[36] S. Bae, J. H. Ahn, C. W. Park, H. K. Son, K. S. Kim, N. K. Lim, C. J. Jeon, H. Kim, *Cell Tissue Res.* **2009**, *335*, 565.
[37] E. Alt, Y. Yan, S. Gehmert, Y.-H. Song, A. Altman, S. Gehmert, D. Vykoukal, X. Bai, *Biol. Cell* **2011**, *103*, 197.
[38] T. E. Ichim, P. O'Heeron, S. Kesari, *J. Transl. Med.* **2018**, *16*, 212.
[39] C. A. Brohem, C. M. De Carvalho, C. L. Radoski, F. C. Santi, M. C. Baptista, B. B. Swinka, C. De, L. R. R. De Araujo, R. M. Graf, I. H. S. Feferman, M. Lorencini, *Int. J. Cosmet. Sci.* **2013**, *35*, 448.
[40] C. M. Teven, X. Liu, N. Hu, N. Tang, S. H. Kim, E. Huang, K. Yang, M. Li, J. L. Gao, H. Liu, R. B. Natale, G. Luther, Q. Luo, L. Wang, R. Rames, Y. Bi, J. Luo, H. H. Luu, R. C. Haydon, R. R. Reid, T. C. He, *Stem Cells Int* **2011**, 201371.
[41] T. Winkler, C. Perka, P. von Roth, A. N. Agres, H. Plage, B. Preininger, M. Pumberger, S. Geissler, E. L. Hagai, R. Ofir, L. Pinzur, E. Eyal, G. Stoltenburg-Didinger, C. Meisel, C. Consentius, M. Streitz, P. Reinke, G. N. Duda, H. D. Volk, *J. Cachexia Sarcopenia Muscle* **2018**, *9*, 880.
[42] F. Berthod, L. Germain, N. Tremblay, F. A. Auger, *J. Cell. Physiol.* **2006**, *207*, 491.
[43] J. S. Heo, Y. Choi, H. S. Kim, H. O. Kim, *Int. J. Mol. Med.* **2016**, *37*, 115.
[44] Y. L. Dorland, A. S. Cornelissen, C. Kuijk, S. Tol, M. Hoogenboezem, J. D. van Buul, M. A. Nolte, C. Voermans, S. Huveneers, *Sci. Rep.* **2019**, *9*, 14401.
[45] L. Teixeira, R. R. Dubielzig, in *Haschek and Rousseaux's Handbook of Toxicologic Pathology*, Elsevier, Amsterdam **2013**, 2095.
[46] J. A. McGrath, J. Uitto, *Rook's Textb. Dermatology Eighth Ed* **2010**, *1*, 34.
[47] K. Chan, C. Mok, *Open Orthop. J.* **2012**, *6*, 449.
[48] Y. S. Zhang, A. Arneri, S. Bersini, S. R. Shin, K. Zhu, Z. Goli-Malekabadi, J. Aleman, C. Colosi, F. Busignani, V. Dell'Erba, C. Bishop, T. Shupe, D. Demarchi, M. Moretti, M. Rasponi, M. R. Dokmeci, A. Atala, A. Khademhosseini, *Biomaterials* **2016**, *110*, 45.
[49] J. S. Miller, K. R. Stevens, M. T. Yang, B. M. Baker, D. H. T. Nguyen, D. M. Cohen, E. Toro, A. A. Chen, P. A. Galie, X. Yu, R. Chaturvedi, S. N. Bhatia, C. S. Chen, *Nat. Mater.* **2012**, *11*, 768.
[50] S. Reinke, S. Geissler, W. R. Taylor, K. Schmidt-Bleek, K. Juelke, V. Schwachmeyer, M. Dahne, T. Hartwig, L. Akyüz, C. Meisel, N. Unterwalder, N. B. Singh, P. Reinke, N. P. Haas, H. D. Volk, G. N. Duda, *Sci. Transl. Med.* **2013**, *5*, 177ra36.
[51] A. I. Van Den Bulcke, B. Bogdanov, N. De Rooze, E. H. Schacht, M. Cornelissen, H. Berghmans, *Biomacromolecules* **2000**, *1*, 31.
[52] H. Shirahama, B. H. Lee, L. P. Tan, N. J. Cho, *Sci. Rep.* **2016**, *6*, 31036.
[53] M. T. Poldervaart, B. Goversen, M. De Ruijter, A. Abbadessa, F. P. W. Melchels, F. C. Öner, W. J. A. Dhert, T. Vermonden, J. Alblas, *PLoS One* **2017**, *12*, e0177628.
[54] E. Majima, W. Schnabep, G. Str, D.- Berlin, B. Ag, *D.- Ludwigshafen* **1991**, *2315*, 2307.
[55] B. D. Fairbanks, M. P. Schwartz, C. N. Bowman, K. S. Anseth, *Biomaterials* **2009**, *30*, 6702.
[56] R. Rezakhaniha, A. Agianniotis, J. T. C. Schrauwen, A. Griffa, D. Sage, C. V. C. Bouten, F. N. Van De Vosse, M. Unser, N. Stergiopulos, *Biomech. Model Mechanobiol.* **2012**, *11*, 461.
[57] J. Schindelin, I. Arganda-Carreras, E. Frise, V. Kaynig, M. Longair, T. Pietzsch, S. Preibisch, C. Rueden, S. Saalfeld, B. Schmid, J. Y. Tinevez, D. J. White, V. Hartenstein, K. Eliceiri, P. Tomancak, A. Cardona, *Nat. Methods* **2012**, *9*, 676.
[58] M. H. Elfarnawany, *Electron. Thesis Diss. Repos.* **2015**, 3106.